

# Broadband Design of Acoustic Metasurfaces for the Stabilization of a Mach 4 Boundary Layer Flow

Rui Zhao

Beijing Institute of Technology

Xiao Liu

Beijing Institute of Technology

Chih-Yung Wen (✉ [cywen@polyu.edu.hk](mailto:cywen@polyu.edu.hk))

The Hong Kong Polytechnic University <https://orcid.org/0000-0002-1181-8786>

Xiaoyong Wang

Chinese Academy of Sciences

---

## Research Article

**Keywords:** Boundary layer stabilization, Acoustic metasurfaces, Mack modes, High-speed flow

**Posted Date:** December 14th, 2021

**DOI:** <https://doi.org/10.21203/rs.3.rs-1140242/v1>

**License:** © ⓘ This work is licensed under a Creative Commons Attribution 4.0 International License.

[Read Full License](#)

---

**Version of Record:** A version of this preprint was published at Advances in Aerodynamics on April 6th, 2022. See the published version at <https://doi.org/10.1186/s42774-022-00106-0>.

# Broadband design of acoustic metasurfaces for the stabilization of a Mach 4 boundary layer flow

Rui Zhao<sup>1</sup>, Xiao Liu<sup>1</sup>, Chihyung Wen<sup>2\*</sup>, Xiaoyong Wang<sup>3</sup>

<sup>1</sup>School of Aerospace Engineering, Beijing Institute of Technology, Beijing 100081, China.

<sup>2</sup>Department of Aeronautical and Aviation Engineering, The Hong Kong Polytechnic University, Kowloon, Hong Kong, China.

<sup>3</sup>State Key Laboratory of High Temperature Gas Dynamics, Institute of Mechanics, Chinese Academy of Science, Beijing 100190, China

## Abstract

A piecewise acoustic metasurface is designed to suppress the first mode while marginally amplifying the Mack second mode in a Mach 4 flat-plate boundary layer (BL) flow. The results of linear stability theory (LST) and the  $e^N$  method demonstrate the stabilization effect and transition delay performance, respectively. However, the direct numerical simulation (DNS) results indicate that the designed broadband acoustic metasurface actually weakly excites the first mode with a slightly larger fluctuating pressure amplitude at the surface, which is in contrast to the analysis of LST. The discrepancies are found to lie in the ‘roughness’ effect caused by the recirculation zones inside the microslits and the alternating expansion and compression waves induced at the slit edges, which significantly amplifies the first mode. For further clarification of the competitive mechanism between the acoustic stabilization and ‘roughness’ destabilization effects of metasurfaces on the first mode, a carefully designed metasurface is installed at the maximum growth rate region, which excites the first mode on the metasurface but inhibits its development downstream.

**Keywords: Boundary layer stabilization; Acoustic metasurfaces; Mack modes; High-speed flow**

## 1 Introduction

High-speed boundary layer (BL) transition is one of the crucial issues for the design of supersonic transports and reentry vehicles. Compared to laminar flow, early transition generates a significant increase in viscous drag and heat flux, which leads to high requirements for thermal protection system (TPS) [1-3]. For high-altitude flights in a low disturbance environment and with negligible surface roughness, it is acknowledged that the transition is due to amplification of unstable modes in the BL [4]. In the case of two-dimensional (2D) or axisymmetric high-speed flows, streamwise instabilities, such as the first mode and Mack second mode, are dominant. The first mode is an inviscid instability wave associated with the generalized inflection point in the BL mean profile, while the Mack second mode belongs to the family of trapped acoustic waves. The first mode is dominant at low Mach numbers, but as the Mach number increases, the Mack second mode leads to the transition [5].

---

\* Correspondence: cywen@polyu.edu.hk

Extensive studies have been performed to stabilize the Mack second mode and inhibit the BL transition [14-19]. Kimmel [6] identified the following categories of transition control techniques that could damp the Mack second mode: (1) passives, such as global or local shaping [6,8], porous coatings [1]; and (2) actives, such as retuned blowing and suction [9], CO<sub>2</sub> injection [10], and plasma actuators [10]. Because of the severe heat fluxes and high temperatures around the high-speed vehicle surface, it is difficult to implement active control techniques, and therefore, passive techniques are of primary interest. Malmuth et al. [5] first proposed the porous coating concept that utilizes the viscosity in narrow pores to efficiently dissipate the acoustic Mack second mode. Fedorov et al. [1] deduced the surface impedance boundary condition to model the acoustic effect of realistic microstructures and applied linear stability theory (LST) to investigate the stabilization effect of various inflow conditions and pore shape parameters. Their theoretical finding was then verified in the GALCIT T-5 shock tunnel [12], with a 5° half-angle sharp cone at free-stream Mach numbers ranging from 4.59 to 6.4. The BL on the half cone covered by the porous surface was mostly laminar, whereas transition was observed halfway along the other half cone with an untreated solid surface. With the motivation that a practical porous coating should be symbiotic with the actual materials of TPS, Fedorov et al. [13] experimentally and theoretically studied the effect of a felt-metal coating with random microstructures on hypersonic BL instabilities and showed that this type of porous coating strongly stabilized the second mode and marginally destabilized the first mode. Maslov [14] experimentally studied the stabilization effects of both regular porous coatings and random felt-metal porous coatings and found that both types stabilized the second mode while the first mode was excited. Wagner et al. [15] pioneered the use of carbon-carbon (C/C), an intermediate state of C/C-SiC already employed in hypersonic vehicles for thermal protection, to control Mack second mode waves. Wind tunnel experiments have been conducted at Mach 7.5, and the stabilization of the second mode as well as an increase in the laminar portion of the BL over the porous surface have been observed [15]. Tu et al. [16] investigated the optimal porosity and pore radius for stabilizing the most unstable second mode waves. Due to the coating's marginal effect on the mean flow and great suppression of the most unstable BL instability, this technique has been widely investigated by theoretical analysis [17-19], wind-tunnel experiments [12,13,19,21,22], and direct numerical simulations (DNS) [23,24]. More updated progresses could be found in Refs. [25-28]. Recently, Zhao et al. [31] expanded the research subjects by introducing the acoustic metasurface concept. Acoustic metasurfaces are planar metamaterial structures constructed with monolayer or multilayer stacks of subwavelength building blocks, which have significantly broadened the horizon of acoustic wave manipulation from wave-front modulation to sound insulation and absorption. According to this definition, the aforementioned porous coating belongs to the absorptive acoustic metasurface. Contrary to the long-held belief that acoustic wave energy dissipation is indispensable in suppressing the Mack second mode, Zhao et al. [31] proposed a nearly nondissipative impedance-near-zero acoustic metasurface, which inhibits the growth of the Mack second mode by the out-of-phase behavior that minimizes the near-surface acoustic pressure. They further designed a reflection-controlled metasurface for suppressing the Mack second mode by controlling the reflection directions of disturbance waves [32].

Compared to the abundance of studies for stabilizing the Mack second mode, there seem to be limited options for controlling the first mode. Kimmel [6] noted that this mode could be stabilized by wall cooling, suction and a favorable pressure gradient. Another way to damp the first mode is to use a very thin perforated sheet stretched over a plenum chamber. When the TS waves propagate along the BL, the fluctuating pressure forces air in and out of the plenum chamber that produces a near-wall region of negative Reynolds stress. Carpenter & Porter [29] conducted LST analyses for the incompressible BL on a flat plate and showed that the TS waves are stabilized when the wall admittance phase is close to  $\pi/2$ . Whether the experiments will confirm the theoretical predictions remains to be seen. They indicated that this theory leads to severe constraints on the perforated sheet thickness, and the pressure variations may lead to areas of quasi-steady inflow and outflow, thereby modifying the mean flow and its stability characteristics. Wang & Zhong [30] analyzed the porous coating admittance and noticed that its phase angle was closely related to the destabilization of the first mode, i.e., the destabilization effect decreased as the phase angle of admittance decreased. However, they used an artificial porous coating boundary for numerical demonstration instead of realistic coating structures. Tian et al. [25] found that the first mode is amplified as the admittance phase  $\theta$  varies from  $0.5\pi$  to  $\pi$ , whereas the second mode is destabilized when  $\theta$  tends to  $0.5\pi$  and suppressed as  $\theta \geq 0.75\pi$ ; furthermore, the stabilization or destabilization effects on Mack modes are intensified by the increase in the amplitude of admittance. Following this principle, they theoretically designed an acoustic metasurface that could damp the second mode in a wide frequency range with the first mode slightly destabilized. Zhao et al. [33] designed a metasurface that suppressed the first mode in a Mach 4 BL flow with the Mack second mode not considered. Furthermore, Wang et al. [35] proposed a broadband design strategy that damps the first mode and Mack second mode in the high-frequency region through LST analyses.

In the present study, a piecewise acoustic metasurface aimed at suppressing the first mode while marginally exciting the Mack second mode is designed by LST and subsequently validated by DNS. This paper is organized as follows. Section 2 introduces the numerical methods employed in the present research. After that, the high-speed BL stabilization problem and broadband design strategy are described in Section 3. Section 4 compares the results from LST and DNS. The discrepancies are further verified and discussed. The conclusions are summarized in Section 5.

## 2 Numerical Methods

In the current research, DNS is employed to directly resolve the detailed BL flow fields among the metasurface microstructures, which are used to verify the effectiveness of the impedance boundary condition when employed in the LST and the stabilization performance of the designed broadband metasurface. The LST and  $e^N$  methods are mainly used to analyze the increment ratio of the unstable modes and determine the transition delay performance on the metasurface.

## 2.1 Direct numerical simulation

The DNS governing equations are two-dimensional (2-D) Navier–Stokes equations in dimensional conservation form:

$$\frac{\partial Q^*}{\partial t^*} + \frac{\partial E^*}{\partial x^*} + \frac{\partial F^*}{\partial y^*} = 0, \quad (1)$$

where  $Q^*$  is a vector of conservative variables and  $E^*$  and  $F^*$  are flux vectors in the  $x$  and  $y$  directions, respectively. These vectors are expressed as

$$Q^* = \begin{Bmatrix} \rho^* \\ \rho^* u^* \\ \rho^* v^* \\ e^* \end{Bmatrix}, \quad E^* = \begin{Bmatrix} \rho^* u^* \\ \rho^* u^{*2} + p^* - \tau_{xx}^* \\ \rho^* u^* v^* - \tau_{xy}^* \\ u^* (e^* + p^*) - u^* \tau_{xx}^* + v^* \tau_{xy}^* - q_x^* \end{Bmatrix}, \quad F^* = \begin{Bmatrix} \rho^* v^* \\ \rho^* u^* v^* - \tau_{xy}^* \\ \rho^* v^{*2} + p^* - \tau_{yy}^* \\ v^* (e^* + p^*) - u^* \tau_{xy}^* + v^* \tau_{yy}^* - q_y^* \end{Bmatrix}. \quad (2)$$

Here,  $\rho^*$  is the density;  $u^*$ ,  $v^*$  are velocity components in Cartesian coordinates;  $e^* = p^*/(\gamma - 1) + \rho^*(u^{*2} + v^{*2})/2$  is the total energy; and  $p^*$  is the pressure. The superscript  $*$  denotes dimensional variables.  $\tau^*$  and  $q^*$  are the stress tensor and heat flux with the components

$$\tau_{xx}^* = 2\mu^* \frac{\partial u^*}{\partial x^*} - \frac{2}{3}\mu^* \left( \frac{\partial u^*}{\partial x^*} + \frac{\partial v^*}{\partial y^*} \right), \quad \tau_{xy}^* = \mu^* \left( \frac{\partial u^*}{\partial y^*} + \frac{\partial v^*}{\partial x^*} \right), \quad \tau_{yy}^* = 2\mu^* \frac{\partial v^*}{\partial y^*} - \frac{2}{3}\mu^* \left( \frac{\partial u^*}{\partial x^*} + \frac{\partial v^*}{\partial y^*} \right), \quad (3)$$

$$q_x^* = -\frac{\mu^* \gamma R}{\text{Pr}(\gamma - 1)} \frac{\partial T^*}{\partial x^*}, \quad q_y^* = -\frac{\mu^* \gamma R}{\text{Pr}(\gamma - 1)} \frac{\partial T^*}{\partial y^*}, \quad (4)$$

where  $T^*$  denotes the temperature. The dynamic viscosity  $\mu^*$  is calculated using Sutherlands law. The specific heat ratio and Prandtl number of perfect gas flows are assumed to be  $\gamma = 1.4$  and  $Pr = 0.72$ , respectively.  $R$  is a constant with  $R = R_0/M$ , where gas constant  $R_0 = 8.314 \text{ J}/(\text{mol} \cdot \text{K})$ ; molar mass  $M = 0.029 \text{ kg/mol}$ .

## 2.2 Linear Stability Theory

In this study, 2-D instabilities are considered, and the small nondimensionalized perturbation is expressed in harmonic wave form:

$$[u', v', p', T']^T = \Psi(y) e^{i(\alpha x - \omega t)} \quad (5)$$

The dimensionless coordinates  $x$  and  $y$  are normalized by the BL thickness scale  $l^* = \sqrt{\mu_e^* x^* / \rho_e^* u_e^*}$ . The flow velocity components  $u^*$ ,  $v^*$ , temperature  $T^*$  and pressure  $p^*$  are normalized by  $u_e^*$ ,  $T_e^*$  and  $\rho_e^* u_e^{*2}$ , respectively. The subscript  $e$  denotes the mean flow variables at the BL edge. In Eq. (5),  $\Psi = [\hat{u}, \hat{v}, \hat{p}, \hat{T}]^T$ ,  $\alpha$  is the dimensionless streamwise wavenumber normalized by  $1/l^*$ , and  $\omega$  is the angular frequency normalized by  $u_e^*/l^*$ . With an assumption of a local-parallel boundary layer, the small disturbances governing equations is derived by substituting disturbance quantities into compressible Navier–Stokes equations and equations of state and then subtracting the mean flow parts. The details can be found in Malik [33]. Substituting Eq. (5) into the disturbances governing equations and neglecting the nonlinear terms yields the linearized dispersion relation

$$L(\alpha, \omega)\Psi = 0 \quad (6)$$

where nonzero elements of the matrix  $L$  are evaluated by the local mean flow velocity and temperature, which can be obtained from a compressible self-similar solution [33]. The boundary conditions are

$$\begin{aligned} \hat{u} = \hat{T} = 0, \hat{v} = A\hat{p}, & \quad y = 0 \\ \hat{u} = \hat{v} = \hat{T} = 0, & \quad y \rightarrow \infty \end{aligned} \quad (7)$$

where  $A$  is admittance of acoustic metasurface. Notably, for a smooth wall,  $A$  is equal to zero.

The spatial theory is able to demonstrate the changes in amplitudes of eigenmodes with distance; therefore, the dispersion problem is converted into a spatial problem, in which  $\omega$  is given and  $\alpha$  is unknown.  $\alpha$  is obtained by employing the single domain spectral collocation method [33]. The growth rate of a wave perturbation is  $\sigma = -\alpha_i$ , where  $\alpha_i$  is the imaginary part of  $\alpha$ . The disturbance wave is unstable with a negative  $\alpha_i$ . A regular acoustic metasurface structure consisting of microslits is shown in Fig. 1, with width  $2b$ , spacing  $s$ , and depth  $H$  nondimensionalized by  $l^*$ .

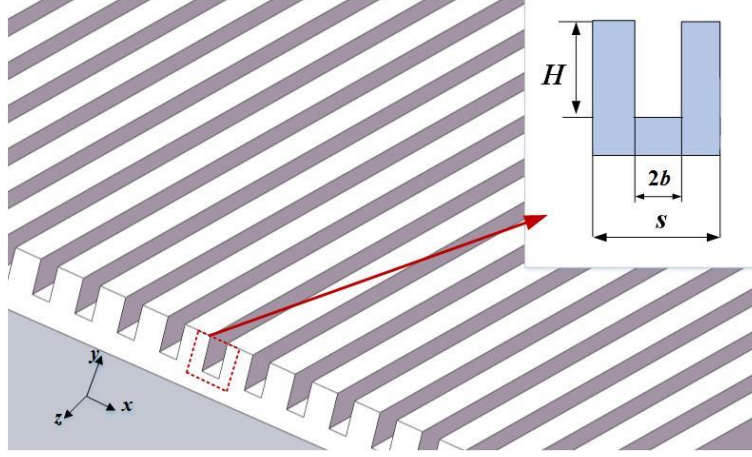


**Fig. 1** Schematic illustration of the acoustic metasurface with subwavelength grooves

The acoustic metasurface admittance for normal incident waves was derived in Ref. [17,36]

$$A = \frac{1}{Z} = nM_e \sqrt{T_w \left(1 - \frac{\tan(k_t b)}{k_v b}\right) \left(1 + \frac{(\gamma-1)\tan(k_t b)}{k_v b}\right)} \tanh \left( i\omega H M_e \sqrt{\tau_w \left(1 - \frac{\tan(k_t b)}{k_v b}\right)} \right) \quad (8)$$

where  $A$  is the metasurface admittance,  $Z$  is the metasurface impedance,  $n$  ( $\equiv 2b/s$ ) is the porosity of the acoustic metasurface, and the dimensionless viscous wavenumber  $k_v$  and thermal wavenumber  $k_t$  are given by  $k_v \equiv \sqrt{i\omega R / (T_w \mu_w)}$  and  $k_t \equiv \sqrt{\text{Pr} k_v}$ , respectively [28]. The admittance of the acoustic metasurface is a complex number and can be expressed as  $A = |A|e^{i\theta}$ , where  $|A|$  denotes the admittance magnitude and  $\theta$  denotes the admittance phase. Accordingly, the disturbance energy flux contributed by the acoustic metasurface per unit area is

$$E_w = \frac{1}{4} (p'_w + c.c.) (v'_w + c.c.) = |A| |p'|^2 \cos(\theta), \quad (9)$$

where  $c.c.$  corresponding complex conjugate. To suppress the disturbances, i.e.,  $E_w < 0$ , the admittance phase angle should be in the range of  $\theta \in [0.5\pi, 1.5\pi]$ .

The  $e^N$  method is a semiempirical method based on LST, which predicts the transition location by accumulating the growth rate of unstable waves [38]. This method is applied to evaluate the transition delay performance by the designed acoustic metasurface. In the  $e^N$  method, the logarithmic amplification ratio of the amplitude versus its initial value for each wave is:

$$N(\omega, x) = \ln(A / A_0) = \int_{x_0}^x \sigma(\omega, x) dx, \quad (10)$$

where  $x_0$  is the location of onset of instability, and  $A_0$  is the disturbance amplitude there. The envelope of these ratios, i.e., the  $N$  factor that represents the amplitude evolution of the most amplified disturbance, is:

$$N(x) \equiv \max_{\omega} N(\omega, x) \quad (11)$$

### 3 Broadband Design Strategy

#### 3.1 Problem Description

In previous studies, an acoustic metasurface was conventionally designed with relatively deep microslits or pores to absorb the acoustic energy of Mack second mode waves [24]. However, the first mode dominates the BL transition at a lower Mach number. In such cases, the acoustic metasurface should be designed to stabilize the first mode while marginally promoting the second mode. The stabilization problem is simplified as a high-speed flat-plate BL flow at zero angle of attack, as shown in Fig. 2 (a). The freestream conditions are as follows: Mach number of 4, temperature of 70 K and unit Reynolds number of  $1.39 \times 10^7 \text{ m}^{-1}$ . The wall is isothermal with temperature of 295 K. The acoustic metasurface is placed at  $0.05 \text{ m} < x^* < 0.4 \text{ m}$  in both LST and DNS calculations. The computation domain above the surface is  $0.48 \text{ m} \times 0.1 \text{ m}$ , which has a grid dimension of  $8618 \times 200$  in the streamwise and vertical directions. We elongated the domain to  $x^* = -0.04 \text{ m}$  with symmetry conditions at  $y^* = 0 \text{ m}$  to avoid numerical instability caused by the singular point at the tip of the flat plate. The computational grid clusters at the leading edge and plate surface with approximately 50 grids within the BL to resolve the disturbance accurately. To achieve global optimum stabilization, the broadband acoustic metasurface is cut into 35 pieces with different sets of geometrical dimensions of microslits (Fig. 2 (b)). According to the grid independence study in Ref. [37], the shallowest slit has a grid dimension of  $10 \times 15$  (width  $\times$  depth), while the deepest slit has a grid dimension of  $15 \times 20$ . The detailed dimensions of broadband acoustic metasurface will be introduced in Sec 3.2 later. For comparison, a conventional metasurface with microslit depth  $H^* = 1.0 \times 10^{-3} \text{ m}$ , width  $2b^* = 1.0 \times 10^{-4} \text{ m}$  (aspect ratio,  $Ar \equiv 2b^* / H^* = 0.1$ ), and porosity  $n (\equiv 2b^* / s^*) = 0.5$  is also meshed with a uniform grid dimension of  $10 \times 30$  (Fig. 2 (c)).

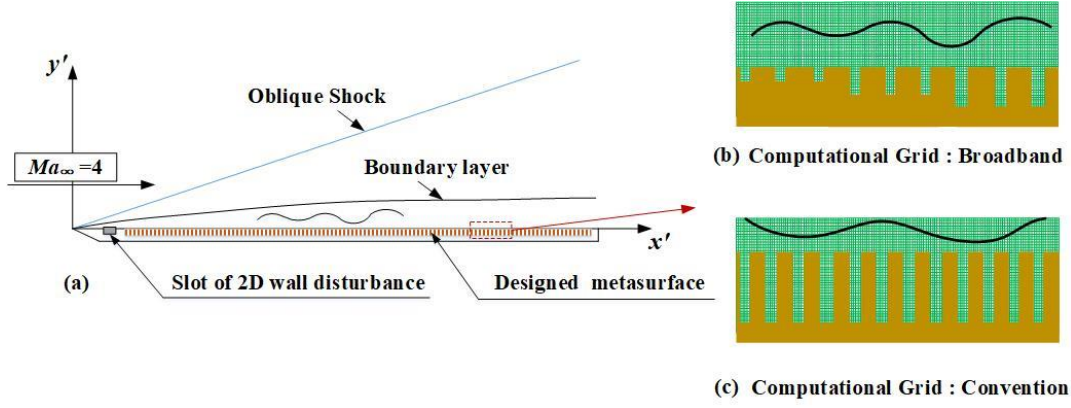


**Fig. 2** Schematic drawing of the problem formulation: (a) high-speed boundary-layer flow, (b) computational grids among the cavities of broadband design, (c) computational grids among the cavities of convention design.

An unsteady disturbance source is introduced in the calculation of DNS by a slot of periodic blowing and suction between  $x_1^* = 0.02$  m and  $x_2^* = 0.03$  m with the expression

$$q_w^*(x^*, t^*) = \varepsilon \rho_\infty^* u_\infty^* \sin\left(2\pi \frac{x^* - x_1^*}{x_2^* - x_1^*}\right) \sin(2\pi f^* t^*), \quad x_1^* \leq x^* \leq x_2^*, \quad (12)$$

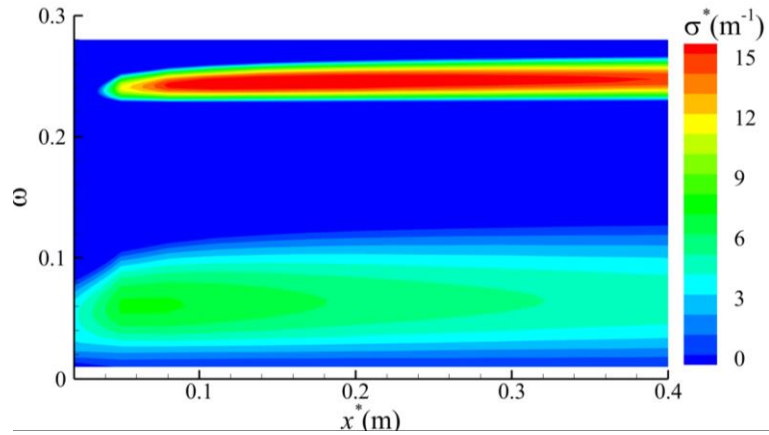
where  $q_w^*$  is the mass flow flux in the normal wall direction. A small forcing amplitude  $\varepsilon = 1.0 \times 10^{-3}$  is adopted, and the forcing frequency  $f^*$  is fixed at 60 kHz. At this frequency, the first mode is gradually amplified along the surface.

### 3.2 Broadband Design Strategy

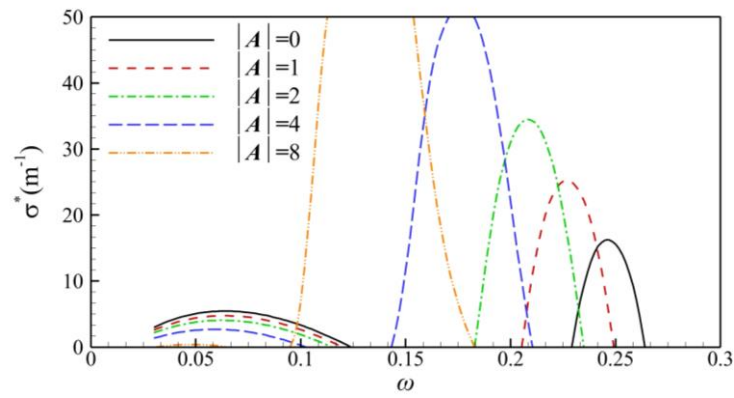
Tian et al. [25] and Wang et al. [35] theoretically investigated the influence of the admittance phase and amplitude on the first and Mack second modes under Mach 4 flow conditions. Tian et al. [25] designed a metasurface with gradient microslits to suppress the second mode across a wide frequency band without distinctly amplifying the first mode. However, the primary concern should focus on the stabilization of the first mode, and the gradient design is challenging for engineering manufacturing. Wang et al. [35] further designed a piecewise acoustic metasurface to obtain the local optimal admittance amplitude and phase to delay transition. The broadband design strategy outlined in Ref. [35] is reviewed below for the sake of completeness.

Fig. 3 shows the growth rates of unstable modes in the BL over the smooth wall analyzed by LST. Both the first mode ( $\omega < 0.12$ ) and second mode ( $\omega > 0.23$ ) coexist in the BL. Since the dimensionless angular frequencies  $\omega$  of their maximum growth rates basically remain constant in the streamwise direction,  $\omega$  can be chosen to characterize the BL instabilities. As shown in Fig. 4, the stabilization or destabilization effect on the unstable modes was closely dependent on the metasurface admittance phase  $\theta$ , and the effect was intensified by an increase in the admittance magnitude  $|A|$ . The first mode is marginally stabilized if  $\theta$  approaches  $0.5\pi$  and is greatly destabilized near  $\theta = \pi$  as  $|A|$  increases. In contrast, the second mode is restrained when  $\theta \geq 0.75\pi$  and amplified as  $\theta$  approaches  $0.5\pi$ . For the present study, the metasurface was cut into 35 pieces in the streamwise direction to enable engineering realization. The admittance  $A$  of each piece should simultaneously meet the following three principles

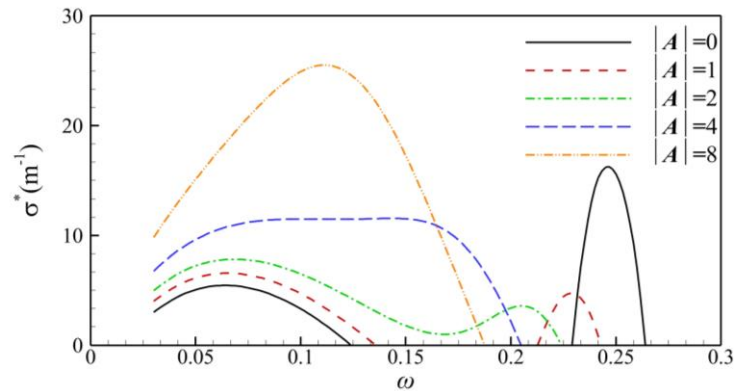
through a careful selection of the geometrical parameters in Eq. (8); that is: 1). As the dimensionless angular frequency  $\omega < 0.12$ , the admittance phase  $\theta$  should be designed to approach  $0.5\pi$  with a small  $|A|$  to ensure the stabilization effect on the first mode (Fig. 4 (a)); 2). in the frequency region where the first and second modes overlap ( $0.12 < \omega < 0.23$ ), for all phases, amplitude  $|A|$  should be designed as small as possible to minimize the destabilization effect on the second mode; 3). When the frequency  $\omega > 0.23$ , the admittance phase should satisfy  $\theta > 0.75\pi$ , and the amplitude effect on the growth rate is negligible (Fig. 4 (b) and (c)).

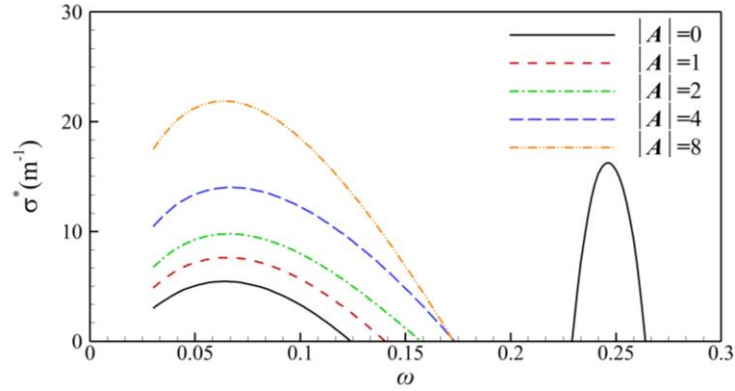


**Fig. 3** Contour of the growth rates of the unstable modes as a function of the dimensionless angular frequencies  $\omega$  and the coordinates along the streamwise  $x^*$  for a smooth solid wall



(a) phase  $\theta = 0.5\pi$



(b) phase  $\theta = 0.75\pi$ (c) phase  $\theta = \pi$ 

**Fig. 4** Effects of the admittance phase and amplitude of the acoustic metasurface on the growth rates of unstable modes ( $|A|=0$  corresponds to the smooth wall).

As shown in Fig. 5, the required geometry parameters are achieved by solving Eq. (8) with program loops in the following order: loop 1 is  $0.1 \times 10^{-3} \text{ m} \leq H^* \leq 1 \times 10^{-3} \text{ m}$ , loop 2 is  $0.1 \leq Ar \leq 1.5$ , and loop 3 is  $0.1 \leq n \leq 0.8$ . These parameters span the range of interest for practical applications. The selected parameters should first satisfy the admittance phase  $\theta$  requirement (Step I in Fig. 5), and then the amplitude  $|A|$  should be small enough to marginally excite the second mode (Step II in Fig. 5). After optimization, the final microstructure parameters at different streamwise directions  $x^*$  are shown in Table 1. The increase in  $H^*$  along the streamwise ensures the stabilization effect on the first and the high-frequency second modes.  $Ar$  increases to 0.7 to detune the admittance phase  $\theta$  to approach  $0.5\pi$  for first mode, whereas a further increasement will lead to the increase in the amplitude  $|A|$ . The porosity  $n$  increases gradually along the streamwise direction, but restrains small values to obtain a small  $|A|$ . For the sake of simplification, the optimization processes are only performed at 7 locations in the streamwise direction, and the optimal parameters are then interpolated into the midpoints of 35 pieces of the designed metasurface.

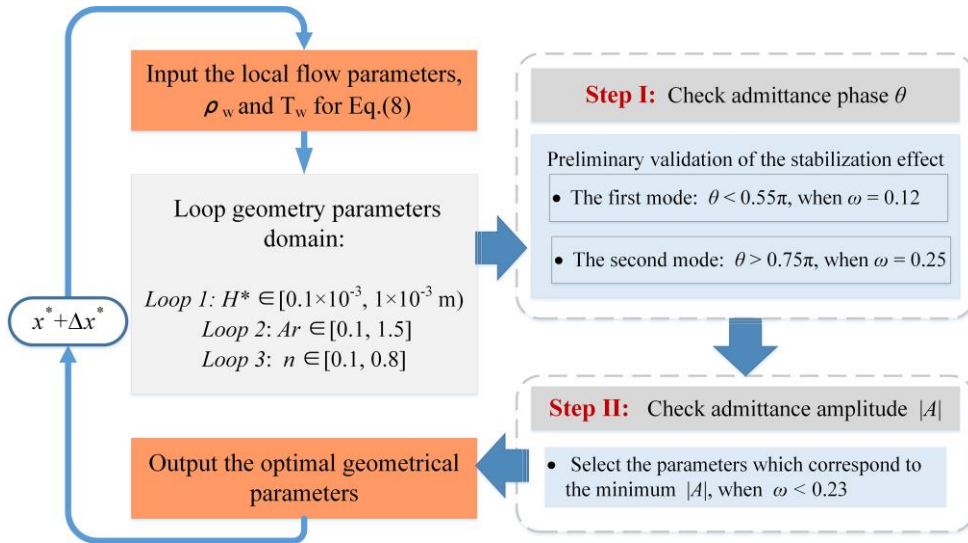


**Fig. 5** Optimal geometric parameters selection method for the broadband metasurface design

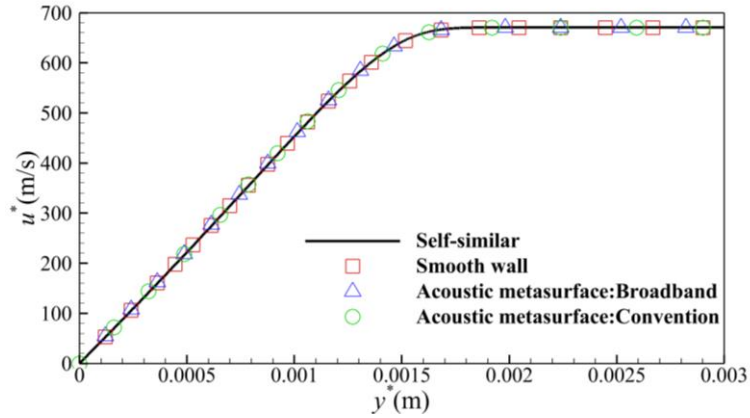
**Table 1** Optimal geometric parameters along the streamwise direction

$x^*(\text{m})$	$H^*(10^{-3} \text{ m})$	$n$	$Ar$
0.10	0.28	0.12	0.7
0.15	0.37	0.12	0.7
0.20	0.44	0.13	0.7
0.25	0.51	0.13	0.7
0.30	0.57	0.14	0.7
0.35	0.63	0.14	0.7
0.40	0.68	0.14	0.7

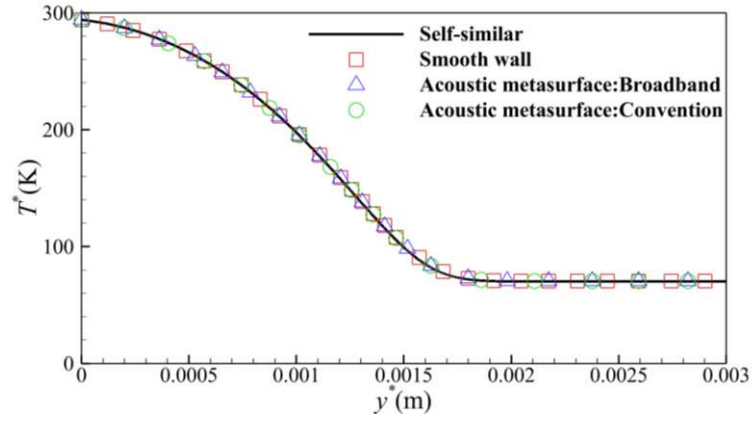
## 4 Results and Discussion

### 4.1 Verification

The accuracy of DNS and the self-similarity compressible Blasius solution used in LST are first verified in the BL flow. As shown in Fig. 6, the profiles of velocity and temperature of DNS are consistent with the self-similar solutions at  $x^* = 0.24 \text{ m}$ . There are no visible discrepancies between the velocity and temperature profiles of smooth walls and the two above-mentioned acoustic metasurfaces, which indicates that acoustic metasurfaces have minimal effects on the mean flow.



(a) Streamwise velocity profile

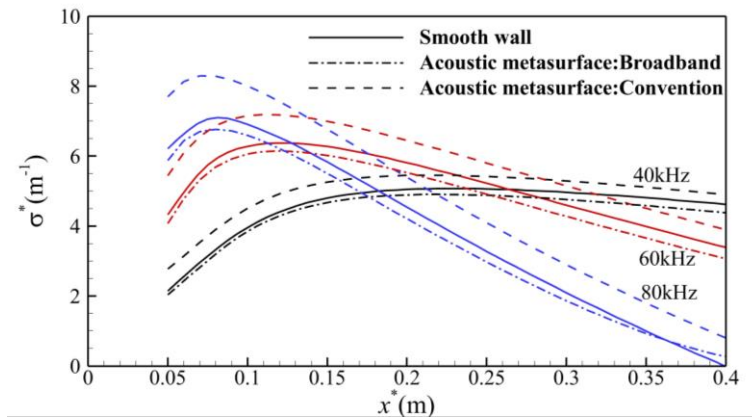


(b) Temperature profiles

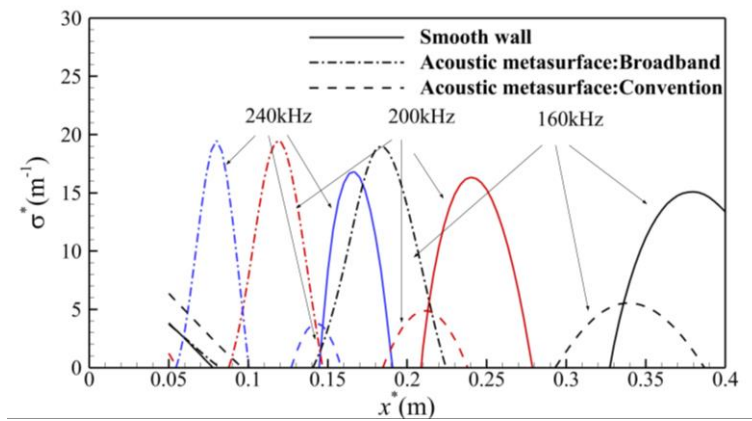
**Fig. 6** Comparisons of streamwise velocity and temperature profiles calculated from DNS and compressible Blasius solution at  $x^* = 0.24$  m above different surfaces.

## 4.2 LST Analysis

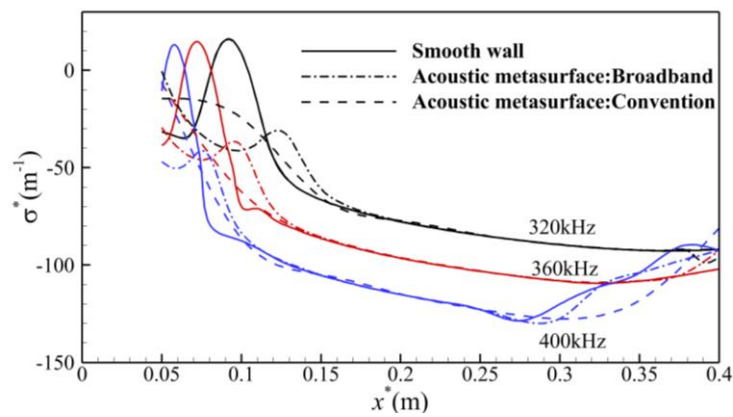
As shown in Fig. 7 (a), the broadband acoustic metasurface successfully damps wide frequencies of first mode disturbances compared with the smooth wall. For Mack second mode disturbances with low frequencies, as depicted in Fig. 7 (b), the designed metasurface weakly enhances the Mack second mode and promotes the position of the maximum growth rate upstream. The growth rates of the high-frequency second mode disturbances become less than zero when two metasurfaces are used, which indicates that the high-frequency disturbance is completely suppressed (Fig. 7 (c)). For comparison, the conventional acoustic metasurface damps all the second mode perturbations but strongly excites the first mode.



(a) the first mode



(b) the second mode of low frequencies



(c) the second mode of high frequencies

**Fig. 7** Dimensional growth rates of unstable modes in the BL along different surfaces

As shown in

Fig. 8, the  $e^N$  method is employed to verify the transition delay performance of the acoustic metasurface. In the frequency range of 40~80 kHz, the broadband acoustic metasurface damps the first mode disturbances, while the conventional metasurface amplifies them. It can also be observed that 60 kHz is the dominant frequency, of which the disturbance reaches the largest  $N$  at the end of the flat plate. With respect to the Mack second mode of low frequencies (160~240 kHz), the  $N$  factor curves of both acoustic metasurfaces move upstream, while the maximum  $N$  factor of the broadband metasurface is only slightly reduced compared to that of the smooth wall. The  $N$  factor in the high-frequency region (320~400 kHz) of both metasurfaces is less than zero, which indicates that both metasurfaces could completely suppress the high-frequency second mode. Figure **Fig. 9** depicts the  $N$ -factor envelopments of different surfaces. Although the  $N$  factor of the broadband acoustic metasurface in the upstream region ( $x^* = 0.05\sim 0.1$  m) is higher than that of the smooth wall, the transition would not be triggered because of the small  $N$  factor. Moving downstream, the  $N$  factor envelopment of the broadband acoustic metasurface is lower than that of the smooth wall, which indicates its potential to delay the transition. In contrast, the conventional one tends to prompt transition with a higher  $N$  factor envelopment under the Mach 4 inflow condition.

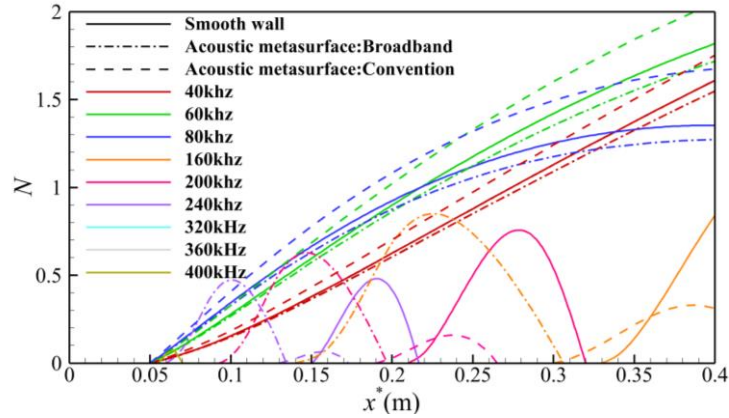


**Fig. 8** Comparison of  $N$ -factor curves of different surfaces

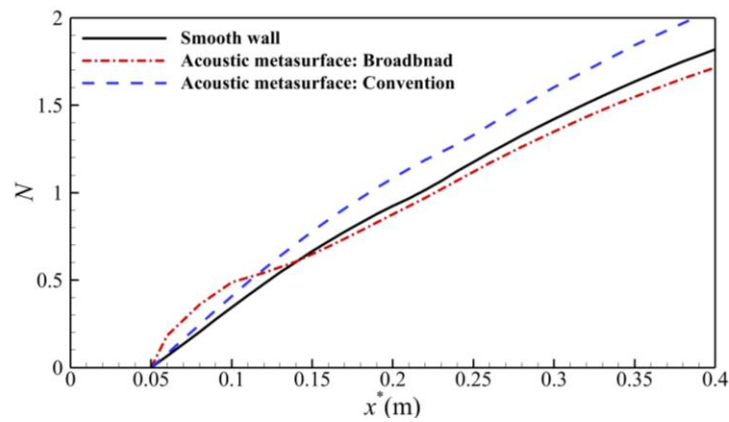


**Fig. 9** Comparison of  $N$ -factor envelopments of different surfaces

### 4.3 DNS Verification

In the above LST analyses, the impedance boundary condition was applied to represent the acoustic effect of the real microstructures on the BL but ignored the recirculation flows inside the slits and the alternating expansion and compression waves induced at the slit edges [37] (Fig. 10). To take into account this simplification, we perform DNS of the broadband and conventional acoustic metasurfaces (see Fig. 2) to verify the stabilization effect at the dominant frequency of 60 kHz. As shown in Fig. 11, compared with the smooth wall, the designed broadband acoustic metasurface actually destabilizes the first modes with larger fluctuating pressure amplitudes at the surface, which is in contrast to the analysis of LST in Sec.4.2 (Fig. 7 (a)). The conventional metasurface largely excites the first mode, as expected. For clarification, the impedance boundary condition for the conventional one is also implemented in DNS for comparison. The impedance model could generally represent the effect of realistic metasurface microstructures for the first mode, but the results are not consistent with the comparisons for the Mack second mode [37]. The fluctuating pressure amplitude is obviously larger in the CFD simulation on the realistic metasurfaces with micro-slits, which indicates that the local flow perturbations would represent a ‘roughness’ effect and excite the first mode. Therefore, it can be concluded that the acoustic metasurface has two opposite influences on the first mode: the acoustic characteristics could be designed to stabilize

the first mode wave, but the very minute local flow perturbation induced by the microstructures will amplify it. This is different from the design of the metasurface for the stabilization of the Mach second mode at higher Mach numbers, wherein the flow perturbances are generally not influential.

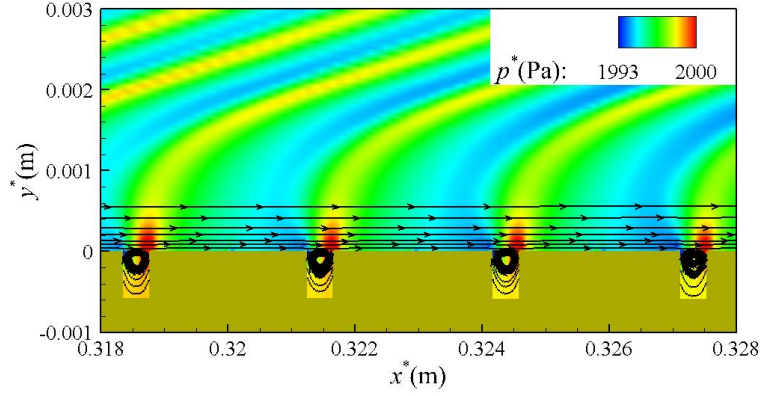


**Fig. 10** Local pressure contour around the cavities of the broadband acoustic metasurface.

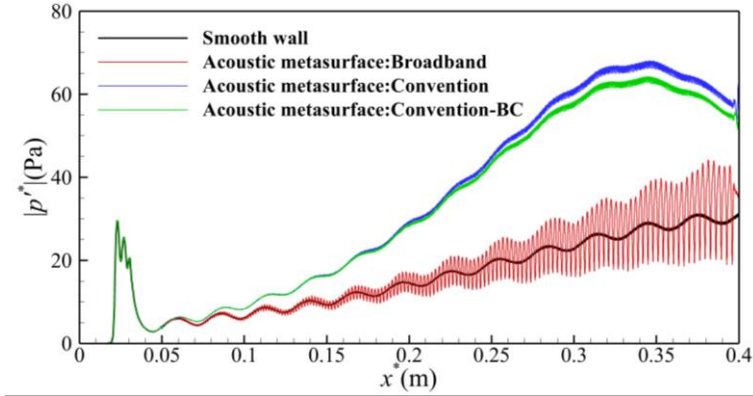


**Fig. 11** Comparisons of wall fluctuating pressure amplitude distributions. (BC: calculated with the impedance boundary condition)

To prove the stabilization effect of the acoustic metasurface on the first mode by DNS, the wall temperature increases to  $T_w=400$  K to further amplify the first mode under the same freestream flow conditions as those in Sec 3.1. The periodic suction-blowing disturbance is chosen to be 80 kHz in the unsteady calculation, which is the dominant frequency of the first mode for this wall temperature condition after LST analysis. The microslits are designed with uniform parameters: depth  $H^* = 4.0 \times 10^{-4}$  m, width  $2b^* = 6.0 \times 10^{-4}$  m, and porosity  $n = 0.536$ . These parameters ensure that the metasurface admittance phase is equal to  $0.52\pi$  to stabilize the first mode at 80 kHz. Fig. 12 shows the disturbance growth rates predicted by LST. The hot wall condition approximately doubles the growth rate of the first mode compared to that in Fig. 7 (a). With the designed metasurface installed along the plate surface ( $0.05 \text{ m} < x^* < 0.4 \text{ m}$ ), the first mode is seen to be significantly suppressed. In the DNS study, the metasurface is only installed at the maximum growth rate region, *i.e.*,  $0.08 \text{ m} < x^* < 0.2 \text{ m}$  to avoid the ‘roughness’ effect on the downstream flow. As shown in Fig. 13, the wall fluctuating pressure amplitudes at the metasurface region are larger than those on the smooth wall, which is contrary to the LST prediction

again. The ‘roughness’ effect of the metasurface plays a dominant role in exciting the first mode. However, the amplitudes gradually decrease downstream of the metasurface, which indicates that the acoustic metasurface could substantially stabilize the amplification process of the first mode. On the other hand, ‘roughness’ is limited to the local influence. The results indicate that the acoustic metasurface should be installed in a confined region where the maximum growth ratio of the first mode occurs to minimize the ‘roughness’ effect.

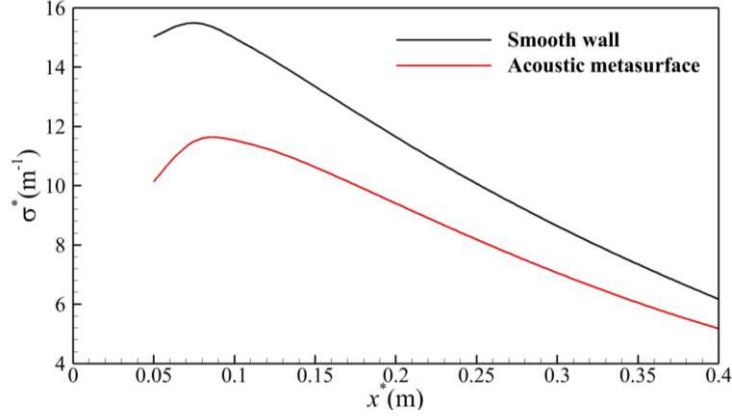


**Fig. 12** Dimensional growth rates along the hot wall with a temperature of 400 K and disturbance frequency of 80 kHz.

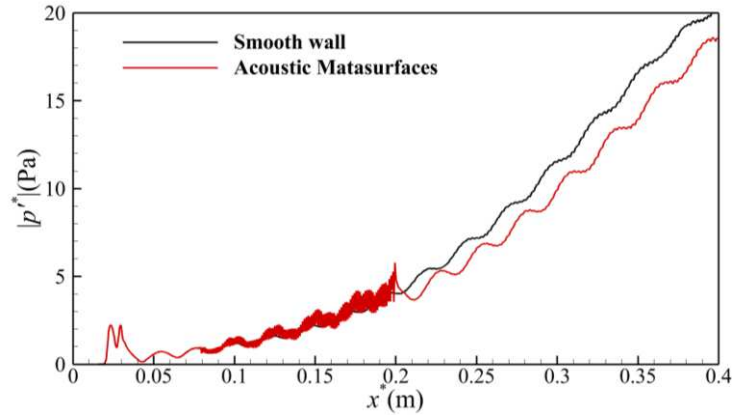


**Fig. 13** Comparisons of fluctuating pressure amplitude distributions along the hot wall with a temperature of 400 K and disturbance frequency of 80 kHz.

## 5 Conclusion

In this paper, a piecewise acoustic metasurface is designed to suppress the first mode across a wide frequency band without amplifying the second mode distinctly in a Mach 4 flat-plate flow. The LST proves its stabilization effect, and the  $e^N$  method demonstrates the trend of delay transition. However, the DNS simulations show contrary results. The discrepancies lie in the neglect of the local flow perturbation caused by the recirculation flows inside the microslits and the alternating expansion and compression waves induced at the slit edges, which behave as ‘roughness’ to excite the first mode. The competitive mechanism between the acoustic stabilization and ‘roughness’ destabilization effect of the metasurface

on the first mode was also found, which was different from that for stabilizing Mack second mode. In the metasurface region, ‘roughness’ plays a leading role in exciting the first mode, while downstream, the disturbance amplification process is inhibited because of acoustic modulation by the metasurface. This not only means that the metasurface microstructures should be carefully designed but also that the installment location should be considered when applying the metasurface to delay the BL transition triggered by the first mode. However, the ‘roughness’ mechanism on the first mode should be further clarified. Additionally, the impedance model should be improved by including the ‘roughness’ effect to reach a consistent result between LST and DNS.

### **Acknowledgments**

We express our honest appreciation to Li Xinliang for his generosity in providing the direct numerical simulation codes.

### **Authors’ contributions**

The research output comes from joint effort. All authors read and approved the final manuscript.

### **Availability of data and materials**

All the datasets are available upon request.

### **Competing interests**

The authors declare that they have no competing interests.

### **Author details**

<sup>1</sup>School of Aerospace Engineering, Beijing Institute of Technology, Beijing 100081, China. <sup>2</sup>Department of Aeronautical and Aviation Engineering, The Hong Kong Polytechnic University, Kowloon, Hong Kong, China. <sup>3</sup>State Key Laboratory of High Temperature Gas Dynamics, Institute of Mechanics, Chinese Academy of Science, Beijing 100190, China.

## **References**

1. Bushnell DM, Hefner JN, Ash RL (2008) Effect of compliant wall motion on turbulent boundary layers. *Phys Fluids* 20(10): S31-S48
2. Fedorov A, Malmuth N, Rasheed A, and Hornung H (2001) Stabilization of Hypersonic Boundary Layers by Porous Coatings. *AIAA J* 39(4): 605-610
3. Riley ZB, Deshmukh R, Miller BA, McNamara JJ, and Casper KM (2016) Characterization of Structural Response to Hypersonic Boundary-Layer Transition. *AIAA J* 54(8): 2418-2431.
4. Reshotko E. (1994). Boundary layer instability, transition and control. *AIAA Paper* 94-0001.
5. Malmuth N, Fedorov A, Shalaev V, Cole J, Khokhlov A, Hites M, and Williams D (2013) Problems in high speed flow prediction relevant to control. *AIAA Paper* 1998-2695

6. Kimmel R (2003) Aspects of Hypersonic Boundary Layer Transition Control. 41st Aerospace Sciences Meeting and Exhibit 6-9 January 2003, Reno, Nevada
7. Malik MR (1989) Prediction and control of transition in supersonic and hypersonic boundary layers. *AIAA J* 27(11): 1487–1493
8. Zhong X, Wang X (2012) Direct Numerical Simulation on the Receptivity, Instability, and Transition of Hypersonic Boundary Layers. *Annu Rev Fluid Mech* 44(1): 527-561
9. Thomas AS (1983) The control of boundary-layer transition using a wave-superposition principle. *J Fluid Mech* 137(1): 233–250
10. Fedorov A, Soudakov V, Leyva IA (2013) Stability analysis of high-speed boundary-layer flow with gas injection. *AIAA Paper* 2014–2498.
11. Riherd M, Roy S, Balachandar S (2014) Local stability effects of plasma actuation on a zero pressure gradient boundary layer. *Theor Comp Fluid Dyn* 28(1): 65-87.
12. Rasheed A, Hornung H, Fedorov A, Malmuth N (2002) Experiments on passive hypervelocity boundary layer control using an ultrasonically absorptive surface. *AIAA J* 40(3): 481–489.
13. Fedorov A, Shipluk AN, Maslov A, Burov E, Malmuth N (2003) Stabilization of a hypersonic boundary layer using an ultrasonically absorptive coating. *J Fluid Mech* 479: 99-124.
14. Maslov A (2003) Experimental and Theoretical Studies of Hypersonic Laminar Flow Control Using Ultrasonically Absorptive Coatings (UAC). Report ISTC 2172-2001, May 2003.
15. Wagner A, Kuhn M, Martinez SJ, Hannemann K (2013) Experiments on passive hypersonic boundary layer control using ultrasonically absorptive carbon-carbon material with random microstructure. *Exp Fluids* 54(10): 1606-1616
16. Tu GH, Chen JQ, Yuan XX (2018) Optimal porosity and pore radius of porous surfaces for damping the second-mode instability. *Acta Aerodynamica Sinica* 36(2): 273-278 (Chinese)
17. Kozlov V, Fedorov A, Malmuth N (2005) Acoustic properties of rarefied gases inside pores of simple geometries. *J Acoust Soc Am* 117(6): 3402-3412
18. Wartemann V, Lüdeke H, Sandham N (2009) Stability analysis of hypersonic boundary layer flow over microporous surfaces, *AIAA Paper* 2009-7202
19. Stephen S, Michael V (2013) Effects of porous walls on hypersonic boundary layers over a sharp cone. *AIAA J* 51(5): 1234-1244
20. Lukashovich S, Maslov A, Shipluk A, Fedorov A, Soudakov V (2012) Stabilization of high-speed boundary layer using porous coatings of various thicknesses. *AIAA J* 50(9): 1897-1904
21. Lukashovich S, Morozov S, Shipluk A (2013) Experimental study of the effect of a passive porous coating on disturbances in a hypersonic boundary layer. 1. Effect of the porous coating length. *J Appl Mech Tech Ph+* 54(4): 572–577
22. Tu GH, Chen JF, Wan B (2019) Investigation on correlation between wind tunnel and flight for boundary layer stability and transition of MF-1 blunt cone. *Scientia Sinica* 49(12): 124701
23. Sandham N, Lüdeke H (2009) Numerical study of Mach 6 boundary-layer stabilization by means of a porous surface. *AIAA J* 47 (9): 2243–2252
24. Brès G A, Colonius T, Fedorov A (2010) Acoustic properties of porous coatings for hypersonic

- boundary-layer control. *AIAA J* 48(2): 267-274
25. Tian X, Zhao R, Long T, Wen CY (2019) Reverse Design of Ultrasonic Absorptive Coating for the Stabilization of Mack Modes. *AIAA J* 57(6): 2264–2269
  26. Xu J, Liu J, Mughal S, Yu P, Bai J (2020) Secondary instability of Mack mode disturbances in hypersonic boundary layers over micro-porous surface. *Phys Fluids* 32(4), 044105.
  27. Fievet R, Deniau H, Brazier JP, Piot E (2020) Numerical study of hypersonic boundary-layer transition delay through second-mode absorption. *AIAA Paper* 2020-2061
  28. Zhu Y, Gu D, Zhu W, Chen S, Lee C, Oran, ES (2021) Dilatational-wave-induced aerodynamic cooling in transitional hypersonic boundary layers. *J Fluid Mech* 911: 1–21
  29. Carpenter PW, Porter LJ (2001) Effects of passive porous walls on boundary-layer instability. *AIAA J* 39 (4): 597–604
  30. Wang X, Zhong X (2011) Phase angle of porous coating admittance and its effect on boundary-layer stabilization. *AIAA Paper* 2011-3080
  31. Zhao R, Liu T, Wen CY, Zhu J, Cheng L (2019) Impedance-Near-Zero Acoustic Metasurface for Hypersonic Boundary-Layer Flow Stabilization. *Phys Rev Appl* 11(4): 5061-5065
  32. Zhao R, Dong Y, Zhang XX, Wen CY, Long TH, Yuan W (2021) Control of Reflected Waves with Acoustic Metasurfaces for Hypersonic Boundary-Layer Stabilization. *AIAA J* 59(6): 1893-1898
  33. Malik MR (1990) Numerical Methods for Hypersonic Boundary Layer Stability. *J Comput Phys* 86(2): 376-413
  34. Zhao R, Yan H, Xi K, Wen CY (2020) Research on Acoustic Metasurfaces for the Suppression of the First Mode. *Aeronautical Science & Technology* 31: 104-112 (Chinese)
  35. Wang WZ, Kong WX, Yan H, Zhao R (2021) Acoustic Metasurfaces for the Stabilization of Broadband Unstable Modes in High Speed Boundary Layer. *J B Univ Aeronaut Astronaut* (Chinese) <https://doi.org/10.13700/j.bh.1001-5965.2021.0235>
  36. Zhao R, Liu T, Wen CY, Zhu J, Cheng L (2018) Theoretical Modeling and Optimization of Porous Coating for Hypersonic Laminar Flow Control. *AIAA J* 56(8): 2942-2946
  37. Zhao R, Wen CY, Long TH, Tian XD, Zhou L, Yuan W (2019) Spatial Direct Numerical Simulation of the Hypersonic Boundary-Layer Stabilization Using Porous Coatings. *AIAA J* 57(1): 1-5
  38. Soudakov V, Fedorov A, Egorov I (2015) Stability of high-speed boundary layer on a sharp cone with localized wall heating or cooling. *Progress in Flight Physics*. vol 7: 569-584